

Searches for continuous gravitational waves from Scorpius X-1 and XTE J1751-305 in LIGO's sixth science run

G.D. Meadors,^{1,2,*} E. Goetz,^{2,3,4,5} K. Riles,⁴ T. Creighton,⁶ and F. Robinet⁷

¹*Albert-Einstein-Institut, Max-Planck-Institut für Gravitationsphysik, D-14476 Potsdam-Golm, Germany*

²*Albert-Einstein-Institut, Max-Planck-Institut für Gravitationsphysik, D-30167 Hannover, Germany*

³*Leibniz Universität Hannover, D-30167 Hannover, Germany*

⁴*University of Michigan, Ann Arbor, MI 48109, USA*

⁵*LIGO Hanford Observatory, Richland, WA 99352, USA*

⁶*The University of Texas Rio Grande Valley, Brownsville, TX 78520, USA*

⁷*LAL, Univ. Paris-Sud, CNRS/IN2P3, Université Paris-Saclay, F-91898 Orsay, France*

(Dated: November 22, 2021)

Scorpius X-1 (Sco X-1) and X-ray transient XTE J1751-305 are Low-Mass X-ray Binaries (LMXBs) that may emit continuous gravitational waves detectable in the band of ground-based interferometric observatories. Neutron stars in LMXBs could reach a torque-balance steady-state equilibrium in which angular momentum addition from infalling matter from the binary companion is balanced by angular momentum loss, conceivably due to gravitational-wave emission. Torque-balance predicts a scale for detectable gravitational-wave strain based on observed X-ray flux. This paper describes a search for Sco X-1 and XTE J1751-305 in LIGO Science Run 6 data using the TwoSpect algorithm, based on searching for orbital modulations in the frequency domain. While no detections are claimed, upper limits on continuous gravitational-wave emission from Sco X-1 are obtained, spanning gravitational wave frequencies from 40 to 2040 Hz and projected semi-major axes from 0.90 to 1.98 light-seconds. These upper limits are injection-validated, equal any previous set in initial LIGO data, and extend over a broader parameter range. At optimal strain sensitivity, achieved at 165 Hz, the 95% confidence level random-polarization upper limit on dimensionless strain h_0 is approximately 1.8×10^{-24} . The closest approach to the torque-balance limit, within a factor of 27, is also at 165 Hz. Upper limits are set in particular narrow frequency bands of interest for J1751-305. These are the first upper limits known to date on r -mode emission from this XTE source. The TwoSpect method will be used in upcoming searches of Advanced LIGO and Virgo data.

PACS numbers: 04.30.-w, 04.30.Tv, 04.40.Dg, 95.30.Sf., 95.75.Pq, 95.85.Sz, 97.60.Jd

I. INTRODUCTION

Non-axisymmetric spinning neutron stars are predicted to emit continuous gravitational waves (GWs) [1]. In particular, Low-Mass X-ray Binaries (LMXBs) may sustain long-lasting non-axisymmetry through accretion onto the constituent neutron star from the binary partner. This accretion may reach a torque-balance, where angular momentum carried away by GW emission equals that added from accretion [2, 3], depending on the ability of the neutron star equation of state to support non-axisymmetric shapes or fluid modes, as well as the absence of other dissipative mechanisms. Scorpius X-1 (Sco X-1), the brightest enduring extrasolar X-ray source [4], is noteworthy: because detectable GW energy flux scales with observed X-ray flux, it is a promising source for the Laser Interferometer Gravitational-wave Observatory (LIGO) and fellow GW observatories [5]. While GW emission due to the $l = m = 2$ mass quadrupole moment is expected at twice the neutron star's spin frequency ($f_0 = 2\nu$), emission may occur at other frequencies in the case of r -mode *Rossby* oscillations [5–8]. Here we carry

out a broadband search for continuous GWs from Sco X-1, as well as narrowband searches for r -modes centered on particular frequencies in the case of X-ray transient XTE J1751-305 for which a sharp spectral line in X-rays has been observed [9] that may be indicative of non-radial oscillation modes (such as r -modes).

GW detector data have been analyzed using various strategies to search for continuous waves [10–15]. The method used here, TwoSpect [16], has been used opportunistically in a previous all-sky analysis to search for Sco X-1 in LIGO Science Run 6 (S6) and the second and third Virgo Science Runs (VSR2 and 3) [17], but it has been subsequently improved (by a factor of $9.5/4.0 = 2.375$ for random polarization [18]) and those improvements demonstrated in a Mock Data Challenge (MDC) of simulated signals [19]. This method searches for evidence of orbital modulation of a continuous narrowband signal in strain data as seen in the time-frequency domain. Upper limits from previous searches for Sco X-1 in initial LIGO data [17, 20–23] have used diverse techniques to calculate upper limits for each algorithm. We produce frequentist upper limits using injections in each band, validating against an extrapolated estimate. Per-band injections yield more conservative limits, which we present, matching the best previous while extending results to a broader band (40 to 2040 Hz). Sco X-1 ephemerides are listed in

* grant.meadors@ligo.org

Table I. Data is used from LIGO Science Run 6 (S6), 2009 July 09 to 2010 October 20, with 4-km-long LIGO Hanford (H1) and LIGO Livingston (L1) detectors, as described in Table II.

Because the spin frequency ν [9, 30] and frequency derivative [31] of XTE J1751-305 are known, its search is significantly less intensive than the search across frequencies required for Sco X-1. This paper will focus on Sco X-1 to illustrate the general case.

II. SEARCH METHOD

Our search method for Sco X-1 and J1751 is derived from an all-sky algorithm, TwoSpect [16, 17], specialized to a single sky location [18].

Orbital motion of binary systems involves multiple parameters beyond an isolated continuous GW source. Here we assume a circular orbit of known orbital period ($P = 2\pi/\Omega$). The algorithm is not sensitive to initial GW phase, nor to orbital phase as manifested by time of ascension T_{asc} , the time epoch of the source crossing the orbital ascending node. Argument of periapsis is also ignored, because orbital eccentricity is small; slight variations could result in biased parameter estimation for signals but should not affect upper limits (see Appendix A). Sky position (α, δ) and period for Sco X-1 are known to sufficient precision [25, 27] to use fixed values in the search [16, 18]. Spindown \dot{f}_0 is presumed small due to torque-balance. Amplitude parameters (strain h_0 , neutron star inclination ι , initial GW phase Φ_0 , and polarization angle ψ) are averaged out through time-dependent antenna functions F_+ and F_\times . The antenna functions depend on the observatories [10].

Given known sky location and period, the search is restricted to two dimensions: f_0 and projected semi-major axis, $a_p = (a \sin i)/c$. ($a \sin i$ is in units of distance, a_p in units of time). Doppler frequency modulation depth, $\Delta f_{\text{obs}} = 2\pi a_p f_0 / P$, is more directly observable than a_p , and template spacing is uniform in Δf_{obs} , so search grids are specified in $(f_0, \Delta f_{\text{obs}})$. These parameters describe the assumed phase evolution, $\Phi(t)$, of the strain $h(t)$ for detector time t and solar-system barycenter time τ :

$$h(t) = \left[F_+ \frac{1 + \cos^2 \iota}{2}, F_\times \cos \iota \right] \begin{bmatrix} h_0 \cos \Phi(t) \\ h_0 \sin \Phi(t) \end{bmatrix}, \quad (1)$$

$$\Phi(t) = \Phi_0 + 2\pi f_0 \tau(t) + \Delta f_{\text{obs}} P \sin(\Omega[t - T_{\text{asc}}]), \quad (2)$$

$$\Delta f_{\text{obs}} \equiv \Omega a_p f_0. \quad (3)$$

A detection statistic, R , is constructed based on the strain power, $|h(t)|^2$. Data is pre-processed into N Short Fourier Transforms (SFTs) of duration T_{coh} indexed by n with frequency bins k . As explained previously [16, 18], the normalized power P_k^n is calculated per SFT, along with its running expectation value, $\langle P_k \rangle^n$. The circular-polarization antenna pattern power, $F_n^2 \equiv F_{+,n}^2 + F_{\times,n}^2$ is

also computed. The normalized, background-subtracted, antenna-function-dependent SFT powers \tilde{P}_k^n are calculated for each (n, k) pixel. Powers \tilde{P}_k^n are then Fourier-transformed by $\mathcal{F}_{f'}$ from the time-domain n to the second-frequency domain, f' , which corresponds to orbital period. Lastly, SFT background noise $\lambda(f')$ is estimated [16]. This yields second-frequency domain power, Z :

$$\tilde{P}_k^n \equiv \frac{F_n^2 (P_k^n - \langle P_k \rangle^n)}{(\langle P_k \rangle^n)^2} \left[\sum_{n'}^N \frac{F_{n'}^4}{(\langle P_k \rangle^{n'})^2} \right]^{-1}, \quad (4)$$

$$Z_k(f') = \frac{|\mathcal{F}_{f'}[\tilde{P}_k^n]|^2}{\langle \lambda(f') \rangle}. \quad (5)$$

We reindex $Z_k(f')$ as Z_i , where i is a pixel index in the (k, f') plane. Each pixel has an expected mean λ_i and a template weight w_i , proportional to the expected magnitude in the presence of a signal. We sort i in decreasing order of w_i and construct the R statistic from the M highest-weighted pixels:

$$R = \frac{\sum_{i=0}^{M-1} w_i [Z_i - \lambda_i]}{\sum_{i=0}^{M-1} [w_i]^2}. \quad (6)$$

The signal model affects the R statistic through w_i , whereas data affects R via Z_i . If one pixel i is dominant, R will approach an exponential distribution; if pixels are equal-magnitude, R will approach a Gaussian normal distribution. As Equations 13-15 of Goetz [16] show, the reconstructed strain amplitude of a signal h_{rec} , is proportional to the quarter-root of R/T_{obs} for fixed $T_{\text{SFT}} = T_{\text{coh}}$. For the same reason, for a fixed duty cycle and a non-transient signal, we expect R to grow linearly with T_{obs} .

Previous, all-sky searches using this program [17] have not calculated the R -statistic for the entire parameter space. Such a calculation was computationally infeasible, because the parameter space included additional dimensions of period and sky location. R was used as a follow-up to an initial, *incoherent harmonic sum* stage. Incoherent harmonic summing involves combining power at each f' with powers at integer multiples of that f' : this approximates an optimal search for any signal that varies periodically, but not necessarily sinusoidally, with period $1/f'$. Because this initial stage's statistic was less sensitive than R , an overall gain in sensitivity is expected from bypassing it for a fully-templated R -statistic analysis, which is feasible for a known source such as Sco X-1. A gain of 2.375 for random polarizations is confirmed by the MDC [18, 19].

For Sco X-1, torque-balance predicts, for a 1.4 solar mass, 10 km radius neutron star [5],

$$h_0 \approx 3.5 \times 10^{-26} (600 \text{ Hz})^{1/2} f_0^{-1/2}. \quad (7)$$

Sco X-1 parameter	Value	Units
Distance (d) [24]	2.8 ± 0.3	kpc
Eccentricity (ϵ) [19]	< 0.068 (3σ)	—
Right ascension (α) [25]	$16:19:55.067 \pm 0.06''$	—
Declination (δ) [25]	$-15^\circ 38' 25.02'' \pm 0.06''$	—
X-ray flux at Earth ($\mathcal{F}_{X\text{-ray}}$) [26]	3.9×10^{-7}	$\text{erg cm}^{-2} \text{ s}^{-1}$
Orbital period (P) [27]	68023.70 ± 0.04	s
Projected semi-major axis (a_p) [28]	1.44 ± 0.18	s

TABLE I. Sco X-1 prior measured parameters from electromagnetic observations (reproduced from methods paper [18]) Note that the projected semi-major axis is in units of time, $a_p = (a \sin i)/c$; the value is derived from a velocity amplitude of $K_1 = 40 \pm 5 \text{ km s}^{-1}$ with uncertainty as understood at the time of the search [19, 20, 27]. Uncertainty has since increased (private communication: derived from the electromagnetically-measured projected radial velocity [29]).

At 50 Hz, $h_0 \approx 1.2 \times 10^{-25}$ represents the high end of likely values [18, 19]. Spin-wandering, or fluctuation in f_0 due to time-varying accretion rate, is expected, but the analysis coherence time T_{coh} is sufficiently short that fluctuations remain within a single Fourier-transform bin and are not likely to affect the search (see Appendix B).

Using 20%-mismatch criteria [16] for the R -statistic we choose a rectangular-spaced search grid in f_0 and Δf_{obs} [18]. Detector noise and computational cost limit the search to $[f_{\text{min}}, f_{\text{max}}] \approx [40, 2040]$ Hz. SFT coherence times T_{coh} are made as long as possible until signals drift out of frequency bins due to Doppler shift from binary orbital motion: 840 s is chosen for $f_0 \in [40, 360]$ Hz and 360 s for $f_0 \in [360, 2040]$ Hz. Shorter SFTs contain a Doppler-modulated signal in-bin for longer portions of the orbit; this is a particular concern for large values of a_p . Analysis is parallelized into jobs of frequency bandwidth $f_{\text{bw}} = 0.1$ Hz; f_{bw} is the maximum feasible given 2 GB RAM per cluster node. Each job covers a_p over $\pm 3\sigma_{a_p}$ by stepping through uniform Δf_{obs} . Equation 6 of the Sco X-1 methods paper [18],

$$\begin{aligned}
 N_{\text{template}} &= 2 \left(T_{\text{coh}} + \frac{1}{f_{\text{bw}}} \right) \\
 &\times \left[1 + \frac{4\pi T_{\text{coh}}}{P} (6\sigma_{a_p})(f_{\text{max}} + f_{\text{min}} + f_{\text{bw}}) \right] \\
 &\times (f_{\text{max}} - f_{\text{min}}). \quad (8)
 \end{aligned}$$

estimates the number of templates required. Evaluated piecewise for $T_{\text{coh}} = 840$ s and 360 s over $[40, 360]$ and $[360, 2040]$ Hz respectively yields 3.7×10^7 and 2.2×10^8 templates per detector. Including the separate analyses of H1 and L1 interferometers, the total is approximately 5.1×10^8 templates. Each template returns the R -statistic, proportional to h_0^4 , along with a single-template $\log_{10} p$ -value.

Simulations are used to set statistical thresholds compatible with the large number of correlated templates. Note that the single-template p -value ceiling is not corrected for a trials factor appropriate to 2000 Hz. This

deficiency, which would need resolution in case of future detection, arises from challenges in estimating the effect of long-range correlated structures [18]. Bonferroni correction (multiplying by the number of templates), is excessively conservative. We defer the issue to a later time, focusing instead on the uncorrected p -value corresponding to a particular empirical false alarm rate. The MDC [19] found that a detection criterion of single-template $\log_{10} p < -7.75$ present with coincidence in two observatories corresponded to a 5-Hz p -value of 0.01. (In the MDC, this 5-Hz p -value was called a false alarm probability of 1% per 5 Hz). In this search, this detection criterion is interpreted instead as a follow-up criterion.

Methods of setting criteria, parameter estimation in case of detection, and upper limits in its absence, are described in [18]. While these methods suffice for Gaussian noise, real detector data contains artifacts. Here we detail detection efficiency and validation of upper limits using simulated signals, *injected* into real data.

When h_0 upper limits are set in noise power spectral density S_H , they can be compared across search algorithms in terms of *sensitivity depth* [32, 33]:

$$D(f) = S_H^{1/2}(f) h_0^{-1}(f). \quad (9)$$

The sensitivity depth of an algorithm is expected to be roughly constant across varying $S_H(f)$ for fixed T_{coh} and with total observing time T_{obs} . Search algorithms with higher sensitivity depth than others, given equal T_{obs} , are said to be more sensitive.

A. Detection efficiency

Detection efficiency is the probability of detecting a signal of a certain strain h_0 . The detector noise floor varies only with f_0 , so we also marginalize over a_p . Although the Doppler parameter a_p is a search dimension, it is spanned by at most $\approx 2.9 \times 10^2$ templates, whereas $\approx 1.7 \times 10^6$ templates are required to span f_0 . Efficiency is calculated for 0.1 Hz-wide bands of frequency f_0 , and

Search parameter	(H1 840-s SFTs)	(L1 840-s SFTs)	(H1 360-s SFTs)	(L1 360-s SFTs)	Units
S6 start	931035615	–	–	–	GPS time (s)
S6 end	971622015	–	–	–	GPS time (s)
Search start	931052760	931052760	931071900	931071660	GPS time (s)
Search end	971621820	971621880	971614500	971614680	GPS time (s)
Duration	40569060	40569120	40542600	40543020	(s)
f_0 start	40.0	40.0	260.0	260.0	(Hz)
f_0 end	360.0	360.0	2040.0	2040.0	(Hz)
Orbital period	68023.8259	–	–	–	(s)
a_p min	0.90	–	–	–	(s)
a_p max	1.98	–	–	–	(s)

TABLE II. Parameters for the Sco X-1 search. Note that different values apply depending on detector (H1, L1) and Short Fourier Transform (SFT) duration $T_{\text{coh}} = (360 \text{ s}, 840 \text{ s})$. Although 360-s SFTs start from 260 Hz, the [260, 360] Hz band results are reported based on more-sensitive 840-s SFTs. Also note that $P = 68023.8259 \text{ s}$ is used in the analysis, based on outdated ephemeris; prior investigations [16] suggest this has negligible effect.

marginalized over Gaussian-distributed a_p ($\sigma_{a_p} = 0.18 \text{ s}$) and P ($\sigma_P = 0.0432 \text{ s}$), as well as uniform-distributed amplitude parameters ($\psi, \Phi_0, \cos \iota$); sky location (α, δ) is fixed, and h_0 is log-uniform over a factor of 50 range that depends on the estimated noise-floor.

For each 0.1-Hz band, 200 signals are simulated. Injections are made for each observatory with appropriate antenna pattern and time delay. A total of 8×10^6 injections are produced (spanning 2000 Hz; 2 detectors). Injections cover a range of amplitude and Doppler parameters. These are aggregated into 1-Hz bands for adequate statistics. Per-injection recovered R -statistics at an injection-centered template, and its immediate neighbors, are compared against the loudest R -statistic in the 0.1-Hz band without injections. Centering the injection recovery grid on the actual injection location may result in a slight overestimate of average detection efficiency. Extrapolation proceeds from an expected mean mismatch $\hat{m} = 1/3$ grid units in any hypercubic lattice [34]. Each grid unit equals the parameter space distance at which mismatch equals a specified level, \bar{m} , for a total mismatch of $m = \bar{m}\hat{m}$. In [34], inspired by the \mathcal{F} -statistic [10], mismatch is a loss in power, h_0^2 , but here, it is a loss in power-squared, h_0^4 . Brady *et al* Equation 5.4 [1] connects an offset signal measured by power, $\tilde{h}(\Delta\lambda)$ to a centered signal, $\tilde{h}(0)$: rearranging, $\tilde{h}(\Delta\lambda) = \tilde{h}(0)\sqrt{1-m}$. ($m \propto (\Delta\lambda)^2$ near a maximum). As the \mathcal{F} -statistic is proportional to $\tilde{h} \propto h_0^2$, but for us $R \propto h_0^4$, we square the $|\tilde{h}(\Delta\lambda)|^2/|\tilde{h}(0)|^2$ term in Equation 5.4 to find our mis-estimate in terms of mismatch: $h_0(\Delta\lambda) = h_0(0)(1-m)^{1/4}$. With our 20% mismatch giving $\bar{m} = 0.2$, the ratio is $(1 - 0.2/3)^{1/4} \approx 0.983$. Therefore, we estimate this effect to be approximately 2%, less than typical calibration uncertainties in previous science runs [35]. Injections with R greater than the loudest R -statistic are classed as ‘detections.’

Detection is expected to become more probable as strain increases, following an approximate sigmoid curve

$s(h_0)$. A two-parameter maximum-likelihood fit is made to $s(h_0)$, from which the 95 % level is estimated analytically. Figure 1 plots detection efficiency in the sample band [165.0, 166.0] Hz.

This injection procedure is not identical to the process for identifying detections in real data. The differences arise from the computational cost of the search and follow-up. In real data, the detection process begins by comparing against the pre-existing threshold from the MDC [18, 19]: those with single-template $\log_{10} p < -7.75$ at both detectors are checked for coincidence. A separate program checks whether $(f_0, \Delta f_{\text{obs}})$ are within a coincidence requirement of $1/T_{\text{coh}}$. Templates that pass are clustered and evaluated in follow-up (Section III A).

B. Upper limits

Absent detections, upper limits at the 95% confidence level ($h_{95\%}$) are the result of the search. Upper limits are taken as the 95% detection efficiency levels, following prior practice [36], computed as in Section II A. Again, 0.1-Hz bands are aggregated into 1-Hz bands for adequate statistics. To find $h_{95\%}$, we take the sigmoid fits $s_K(h_0)$ for observatory K for a given bin, and analytically invert to obtain h_0 for $s_K = 0.95$, and choose the minimum between the two observatories K . This is then repeated for each 1-Hz bin.

Validation is performed by taking a band (or limited set of bands), estimating in each band the multiplier needed to convert R into h_0 , applying that multiplier to the loudest template in all other bands, and comparing that product to the $h_{95\%}$ found above. The initial set of bands examined was [142.0, 143.0] Hz, [162.0, 163.0] Hz, and [222.0, 223.0] Hz, with a preliminary set of injections. To minimize disturbances, [142.0, 142.7] Hz was focused on with the final injection set. This validation is shown in Figure 2, with an independent set of 700 injections in

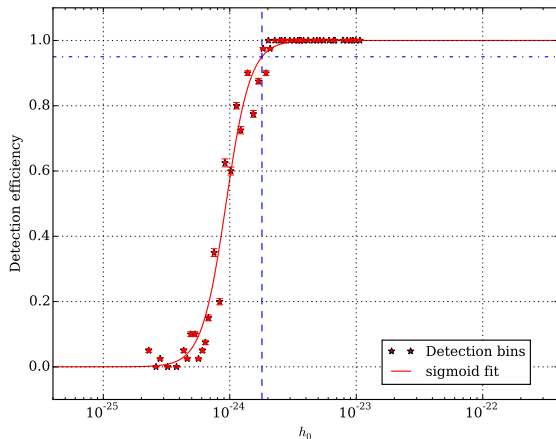


FIG. 1. Detection efficiency of 2000 injections into H1 data over [165.0, 166.0] Hz, with varying amplitude and Doppler parameters. A maximum-likelihood sigmoid fit is made to the unbinned sigmoid distribution of detected/non-detected injections (based on a threshold of $\log_{10} p < -7.75$); the figure shows binned detection probability estimates for illustration purposes only. The strain value (*dashed vertical blue line*) yielding 95% efficiency (*dashed-and-dotted horizontal blue line*) determines the strain upper limit in this band.

[142.0, 142.7] Hz.

For validation, amplitude parameters, particularly $\cos \iota$, induce systematic uncertainty into the estimation of h_0 . At low values of h_0 , TwoSpect cannot resolve injections from the noise, and the slope of Figure 2 is flat. At higher values of h_0 , it recovers injections with $h_{\text{rec}} \propto R^{1/4}$, linearly proportional to the true value. Strain estimates, h_0 , must be determined using h_{rec} with respect to a stated confidence level and injection population. In the figure, the estimated h_0 is plotted. This h_0 is estimated with the smallest coefficient ρ_{UL} such that 95% of $\rho_{\text{UL}} h_{\text{rec}}$ for injections, at any value of strain, are greater than or equal to the true h_0 . The conversion factor necessary is $\rho_{\text{UL}} \approx 4.00$. Moreover, ρ_{UL} can be factored as $2.3 \times \rho_{\cos \iota}$, where $\rho_{\cos \iota} = 1.74(\pm 0.37)$ is a population-dependent estimate of the average ratio of true h_0 to recovered h_0 given a uniform distribution of $\cos \iota$ [18, 19].

The results of multiplying the loudest template h_{rec} in all other bands by ρ_{UL} are generally consistent with the $h_{95\%}$ found by the detection-efficiency method. Variation is expected, since the former is an extrapolation from the ρ_{UL} estimated for [142.0, 142.7] Hz being uniformly applied across all other bands. Such variation is permissible when the detection-efficiency method is more conservative. Agreement can be quantified by comparing the median $\rho_{\text{UL}} h_{\text{rec},i}$ of 10 validation bins, 0.1 Hz each, to the corresponding 1-Hz detection-efficiency bin, $h_{95\%,i}$. Where r is the ratio $\rho_{\text{UL}} h_{\text{rec},i} / h_{95\%,i}$, the median $r = 0.755$, mean 0.753 with standard deviation 0.153. At the most sensitive frequency, $r = 0.898$, whereas the 40-

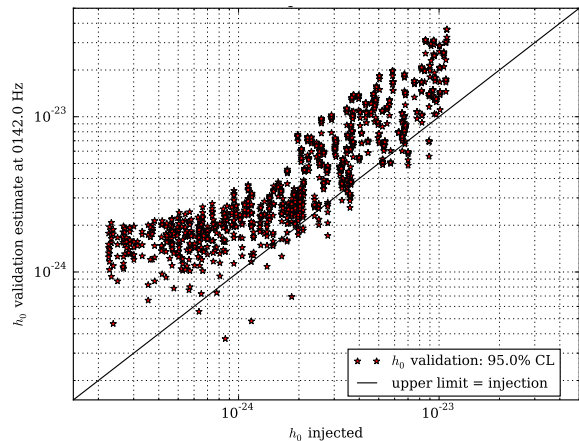


FIG. 2. Upper limit validation, estimated h_0 vs injected h_0 : 700 injections into S6 data in the [142.0, 142.7] Hz band. The uncalibrated ‘recovered’ strain, h_{rec} , must be calibrated by scaling to an ‘estimated’ $h_0 = \rho_{\text{UL}} h_{\text{rec}}$ such that it is greater than or equal to injected h_0 at least 95% of the time (*red points*). This must hold for all values of h_0 . Applying the scaling factor to the loudest outlier in each band, as described in the text, yields a result consistent with the final 95% detection efficiency levels, exemplified by Figure 1, thus validating the upper limits.

50 Hz mean $r = 0.851$ and 2030-2040 Hz mean $r = 0.692$. The tendency for smaller r at high frequency may stem from the higher trials factor as f increases, requiring a search over a larger Δf_{obs} space. As $h_{95\%}$ is larger and more conservative on average, the upper limits are validated.

Upper limits can be set for most frequency bands. A few bands are consistently too noisy, as identified by statistical tests, and therefore cannot be analyzed. SFTs must pass a Kolmogorov-Smirnov and Kuiper’s test: non-Gaussian or anomalously noisy data are not used. These tests are detailed in the TwoSpect all-sky observational paper [17]. For the Sco X-1 search, the 60 Hz and first three harmonic lines at (120, 180, 240) Hz, as well as frequencies near the violin modes around 340 to 350 Hz, are thus excluded [37]. The 40 to 360 Hz H1 and L1 searches excluded cumulative bandwidths of 16.4 Hz and 16.2 Hz respectively, while the 360 to 2040 Hz H1 search excluded 21.4 Hz and L1 16.9 Hz. For generating upper limits, only 288 bins (0.1 Hz each) could not be analyzed with data from either interferometer. Aggregating into 1-Hz bins allows setting upper limits even near many of the disturbances, in some sense recovering the bandwidth at the cost of coarser results, by having more injections for better sigmoid fit statistics. Only 5 aggregated bins of 1 Hz each could not be determined from either interferometer. Results are detailed in Section III B.

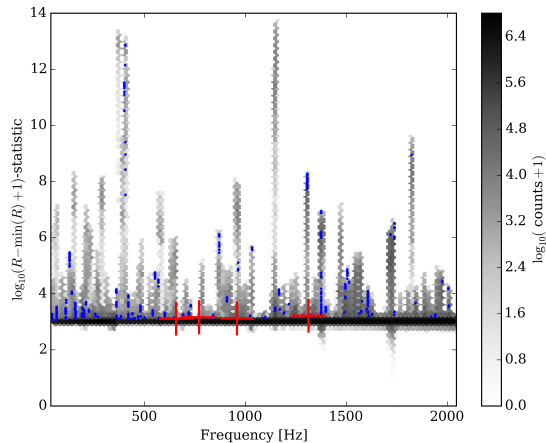


FIG. 3. 2D histogram with hexagonal bins of logarithmic R -statistic versus frequency f_0 for the Sco X-1 S6 search. Histogram for all templates (*gray hex bins*) and followed-up coincident templates only (*blue dots*). Variance in R increases with f_0 , because more pixels are incorporated into the statistic. However, R remains zero-mean. Line artifacts are present at many frequencies, extending to $R \approx 5 \times 10^{13}$. The four outliers from Table III are marked (*red crosshairs*); they are at 656, 770, 957, and 1312 Hz.

III. SCO X-1 RESULTS

Summary results for the R -statistic and estimated single-template p -value of the Sco X-1 search can be found in Figure 3 through 5. These histograms of the data show structural features for both the entire set of templates as well as those passing threshold and coincidence requirements.

A. Sco X-1 outliers

Templates matching the statistical threshold in both observatories and coincident within $1/T_{\text{coh}}$ in both f_0 and Δf_{obs} are clustered together. Because f_0 is a much larger dimension in our search than Δf_{obs} , only f_0 is used to define clusters: any points within twice the maximum possible modulation depth (to allow for degeneracies in the parameter space: points on the same a_p vs f structure [18]) plus 5 SFT bins (for safety with FFT signal leakage [16]) are considered a cluster. Of the 90 clustered outliers in Appendix C, Table VI, 86 are dismissed by visual inspection of the amplitude spectral density in the band. Most show identifiable artifacts, such as instrumental lines and power harmonics. Table III presents four outliers, present in both interferometers between 40 and 2040 Hz, that do not overlap identifiable artifacts.

Of the surviving four outliers in Table III, all except the last (outlier 66, 1312.453 Hz) can be dismissed by coherently summing SFTs before calculating the R -

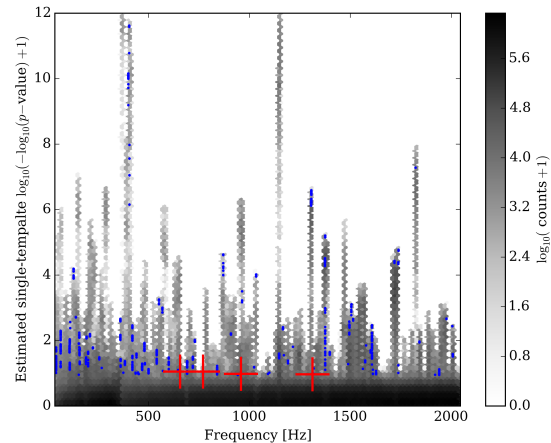


FIG. 4. 2D histogram with hexagonal bins of doubly-logarithmic (single-template) p -value versus frequency f_0 for the Sco X-1 S6 search. Histogram for all templates (*gray hex bins*) and followed-up coincident templates only (*blue dots*). Line artifacts align with those in Figure 3. The four outliers from Table III are marked (*red crosshairs*); they are at 656, 770, 957, and 1312 Hz.

statistic. In this case, when H1 and L1 are in simultaneous operation, SFTs from both are phase-shifted to account for detector separation, the matched SFTs are added together, and then analysis proceeds as for a single (virtual) detector. Real signals are expected to yield higher R -statistics using the coherent sum. This results in higher sensitivity: an H1-L1 sum with unknown $\cos \iota$ and ψ should improve by approximately 29 percent [38] over single-detector analyses, in the all-sky search. Directed searches, such as Sco X-1, are not fully characterized, nor are the false alarm and false dismissal probabilities of the test for higher joint- R , but the example of the \mathcal{F} -statistic multi-detector statistic [39] is informative. The single-detector \mathcal{F} -statistic [10] has an expected statistic, \mathcal{F} , proportional to a non-centrality parameter $\rho \propto h^2$; with N combined detectors, $\rho \propto N$, so sensitivity to h scales like \sqrt{N} . Einstein@Home, for example, vetoes candidates for which any single-detector statistic is less than the joint-detector statistic (the \mathcal{F} -statistic consistency veto) [40]. Because R is not coherent, it will scale more slowly than \mathcal{F} , but should grow with additional detectors. Only the last outlier, 1312.453 Hz, does have a larger R with coherent-summing.

Multiple considerations suggest that the 1312.453 Hz outlier is nevertheless not a real signal from Sco X-1. First, note that the follow-up criterion, as noted in Section II, yield a false alarm probability of 1% per 5 Hz band in Gaussian noise [19]. The data set contains 400 bands of 5 Hz, implying a $(1 - 0.99^{400}) = 0.98$ probability of at least one false alarm. Given the high false alarm probability of the search's follow-up criterion, it is less likely that any particular outlier arises from actual GW

H1 f_0 (Hz)	L1 f_0 (Hz)	H1 Δf_{obs} (Hz)	L1 Δf_{obs} (Hz)	H1 h_0	L1 h_0	Comment
656.6431	656.6458	0.0650	0.0630	1.48×10^{-24}	1.86×10^{-24}	dismissed by coherent sum
770.2250	770.2264	0.1229	0.1256	2.04×10^{-24}	2.46×10^{-24}	dismissed by coherent sum
957.6972	957.6958	0.0803	0.0817	2.24×10^{-24}	2.88×10^{-24}	dismissed by coherent sum
1312.4542	1312.4528	0.2373	0.2380	3.77×10^{-24}	4.53×10^{-24}	fluctuation (see below)

TABLE III. Estimated parameters of outliers not corresponding to obvious artifacts. Frequency f_0 , modulation depth Δf_{obs} , and naive recovered h_0 are shown. 86 of 90 outliers (clustered templates matching threshold in both H1 and L1) can be easily dismissed due to artifacts or visible disturbances in the amplitude spectral density. These 4 remaining outliers survive. Three are dismissed by failing the test of having a higher statistic in when SFTs are coherently summed. The last is highly unphysical, not self-consistent, and statistically marginal, as described in the text. Full outlier listing in Table VI.

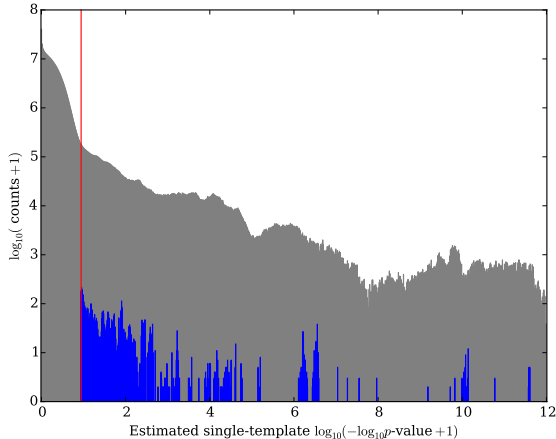


FIG. 5. Doubly-logarithmic horizontal scale for the distribution of $-\log_{10}(p)$ -values. Histogram for all templates (*gray*) and followed-up coincident templates only (*blue*). For high values, $-\log_{10}(p) \propto R$. Note that these extreme values of R are, as shown in Figure 4, typically related to line artifacts in the data. Follow-up threshold of $\log_{10} p = -7.75$ shown in (*red*): a template in each observatory must reach this threshold and be coincident with the other observatory to qualify for follow-up. In comparison to theoretical expectations, templates with many equally-weighted pixels would have Gaussian-distributed R , while templates dominated by a single pixel will have exponentially-distributed R . On this figure's axes, both such distributions would appear as concave-downward curves. The knee in the slope and extended right tail imply that extreme $-\log_{10}(p)$ -values are part of distinct, unmodeled populations, such as the aforementioned line artifacts. In the absence of artifacts or signals, the below-threshold slope would continue.

emission from Sco X-1 (presumed to be monochromatic and with no confusion from GW backgrounds). Moreover, the R -statistic of this outlier does not grow linearly in time if the observation is subdivided. Indeed, subdividing into quarters or thirds yields inconsistent results for the time interval with the loudest R , compared to dividing into halves. These results are also inconsistent with the expectations that $R \propto T_{\text{obs}}$ and the corollary that detectable h_0 scales with $T_{\text{obs}}^{-1/4}$ (see Equation 6 and

below). It is possible, however, that the marginal nature of the outlier elevates the false dismissal probability of this test.

Alternately, Sco X-1 might not be in torque-balance. Then previous assumptions might not apply, and a transient signal for part of the run could not be ruled out. The recovered strain h_{rec} is at least 159 times larger than torque-balance: 2.37×10^{-26} according to prior formulae based on the X-ray flux [5, 18]. (The true strain h_0 , after correcting for $\cos \iota$, would be even larger on average). Hence, spin-down would occur at an estimated rate of at least 3.2×10^{-7} Hz/s (4% of a frequency bin per coherence time; 4674 bins during the observing time). This rapid frequency drift should induce either an extended cluster of outliers at various frequencies consistent with evolution during the run, or else might fail to produce an outlier at all, if the accumulated power in each bin is insufficient. Both possibilities are inconsistent with observed results, so the signal is presumably unphysical.

Although the possibility remains open for a signal at h_0 greater than torque-balance predictions, it would require more statistically consistent evidence to substantiate – the false alarm probability of the search and the inconsistent behavior of the R -statistic do not provide this evidence. Statistical fluctuation is the most likely explanation for the 1312.453 Hz outlier: we conclude that no signals from Sco X-1 have been detected.

B. Sco X-1 random-polarization upper limits

Upper limits (ULs) for the [40, 2040] Hz spectrum, with 95% confidence given random polarization, in units of dimensionless strain, are shown in Figure 6, produced as explained in Section II B. The minimum value, 1.8×10^{-24} , is achieved at 165 Hz: it is approximately 27 times the torque-balance strain limit at that frequency.

Previous Radiometer searches using LIGO Science Run S5 data [21] must be converted for comparison. Note that although S6 noise was improved over S5, the observation time T_{obs} of S5 was approximately twice as long as S6. Whereas both searches should improve proportional to the quarter root of T_{obs} , these effects approximately cancel. The Radiometer UL is calculated for 90% confidence given circular (optimal) rather than

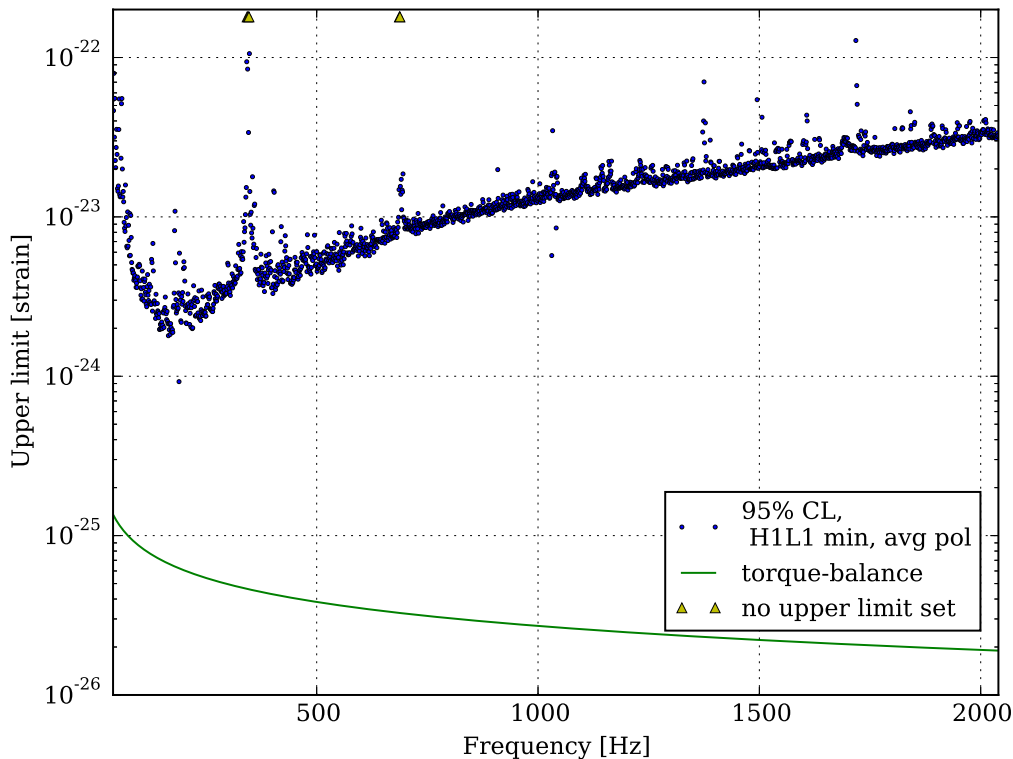


FIG. 6. Upper limit for average (random) polarization GW from Sco X-1 in S6, joint H1-L1, at 95% confidence (*blue dots*). Validated by determining the 95% detection efficiency in injections, this spectrum covers [40, 2040] Hz, using the lower upper limit from either observatory when both yielded results. Results are for 1-Hz bands (closed lower edge, open upper edge). Three bands (189, 1031, and 1041 Hz) have anomalously low upper-limit that probably stem from spectral artifacts visible the run-averaged SFT amplitude spectral density. Five near-overlapping bands total are marked (*yellow triangles*) where upper limits could not be set: four (343, 347, 687 and 688) Hz could not be fit because of additional artifacts yielding insufficient data for the search method, and 345 Hz could not be numerically determined by maximum likelihood. The region around 345 Hz contains the first harmonic of the interferometer suspension violin mode, responsible for these disturbances. Bifurcation in high-frequency limits arises from certain bands being contaminated in H1 and limit being set by the less-sensitive L1 interferometer. Results make no assumptions on $\cos \iota$. Note: torque-balance (*green line*) assumes a 1.4 solar mass, 10 km neutron star.

random polarization; it is presented in units of h_{RMS} , which do not directly correspond to physical strain. Signal leakage across the 0.25 Hz Radiometer bins affects h_{RMS} near the boundaries of bins for signals below 538 Hz (and all signals above) [19]. The effects of signal leakage and polarization dependence have been investigated and found to scale $h_{\text{RMS}} \approx 0.48h_0$, on average, over the range of [50, 1500] Hz [19]. For a specific $df = 0.25$ -Hz bin, the conversion is $h_0 = C_{\text{cp}} \times \sqrt{C_{\text{mbf}} \times \hat{Y}_{\text{tot}} df}$, where $C_{\text{cp}} = 1.74 \pm 0.37$ and C_{mbf} (frequency-dependent) are new with respect to S5. Applying factors of 1.74 and $C_{\text{mbf}}(160\text{Hz}) = (1.2)^{1/2}$ to the best claimed Radiometer result, $h_{\text{RMS}} = 7 \times 10^{-25}$ near 160 Hz, implies the 90%-confidence S5 upper limit was $h_0^{90\%} \approx 1.3 \times 10^{-24}$. Compare the average factor, $(0.48)^{-1} \times 7 \times 10^{-25} = 1.5 \times 10^{-24}$, or the Sideband group's estimated conversion factor [23],

$(2.43) \times 7 \times 10^{-25} = 1.7 \times 10^{-24}$. We can estimate our 90%-confidence levels for direct comparison. The 165 Hz detection efficiency sigmoid (Figure 1) that yields our best upper limits likewise reaches 0.90 at approximately 1.5×10^{-24} in a 1-Hz bin group. Our 0.1-Hz injection sets do not facilitate 0.25-Hz Radiometer bins, but grouping by 0.3-Hz for sigmoid fits yields 90%-confidence limits of $(1.3 \times 10^{-24}, 1.7 \times 10^{-24}, 1.6 \times 10^{-24})$ for bands respectively starting (165.0, 165.3, 165.6) Hz. We believe our limits to be at least comparable to the Radiometer S5 limits, but spanning a broader frequency range and more rigorously calculated, using Monte Carlo injections for the full range of astrophysical polarizations, presented in physical units of strain h_0 at 95% confidence.

Sideband searches in S5 data [23] are more analogous. However, the S5 UL is produced using a Bayesian method different from the MDC and from our frequentist Monte

Carlo injections; some discrepancy may thus arise. The Sideband UL over the range [50, 550] Hz is calculated at 95% confidence, including both random polarization, as here, as well as a restricted prior. Its semicoherent (sensitivity $\propto T_{\text{obs}}^{1/2}$) analysis spans 10 days. When comparing these results, note that the Sideband paper uses the median UL from within a 1 Hz band. Our method instead generates a single UL for each 1 Hz band. As this means that each fit in the current paper may be adversely affected by noise within the band, the quantities are not directly equivalent. For example, calculating 95%-sigmoid ULs from our 0.1-Hz bins and taking the median for [165.0, 165.9]-Hz yields a median of 1.66×10^{-24} compared to our stated UL of 1.8×10^{-24} on the sigmoid for the whole 1 Hz. The UL at our most sensitive frequency, 165 Hz, is nevertheless between the median (1.3×10^{-24}) and worst Sideband UL at its most sensitive frequency, 150 Hz. Moreover, the results in the current paper cover a broader range of [40, 2040] Hz.

While method differences still complicate comparison, we find our ULs to be within factor of 1.4 between Radiometer S5 and Sideband S5 limits; while not distinctly better in sensitivity, they span a larger parameter space (2 kHz in f_0) in S6 data.

IV. XTE J1751-305

A. XTE J1751-305 method

Discovered in 2002 [30], the X-ray transient J1751-305 is another binary system with potential for continuous GW emission. In 2014 [9], X-ray observations of J1751 were reported that exhibited signs consistent with non-radial oscillation modes, such as r - (and *gravity g*-) modes. Debate ensued; an r -mode might have already spun J1751 down below detectable levels [41], but a crust-only surface r -mode might not and could still be present [42]. J1751 is thus an interesting candidate for an opportunistic search well-suited to our method.

J1751 has the shortest known orbital period of any X-ray binary: $P \approx 2545.3$ s. Its semi-major axis is $a_p \approx 0.010$ s. Crucially, its spin frequency is known: $\nu = 435.31799$ Hz. J1751 is distant, at an estimated $d > 7$ kpc, near the galactic center. We consider GW emission at the spin frequency $f_0 = \nu$, the relativistic-corrected r -mode frequency $f_0 = (2 - 0.5727597)\nu$ [9] (dependent on the unknown equation of state), and the quadrupolar frequency $f_0 = 2\nu$. Bands of $f_{\text{band}} = 2.0$ Hz, centered approximately on each frequency, and $a_p \pm 0.0033$ s, are selected with a single period $P = 2545.3414$ s. The search is run on 200-s and 240-s SFTs to cope with high Doppler acceleration from the short P . This analysis overcovers uncertainties, yet is practical ($< 10^5$ templates) for a single-processor in less than a day. Parameters are listed in Table IV.

XTE J1751-305 parameter	Value	Units
Distance (d) [30]	> 7	kpc
Eccentricity (ϵ) [30]	$< 1.7 \times 10^{-3}$	—
Right ascension (α) [30]	$17:51:13.49 \pm 0.05''$	—
Declination (δ) [30]	$-30^\circ 37' 23.4'' \pm 0.6''$	—
Orbital period (P) [30]	2545.3414 ± 0.0038	s
Proj. semi-major axis (a_p) [30]	10.1134 ± 0.0083	ms
Frequency derivative $\dot{\nu}_{\text{spin}}$ [31]	$-0.55(12) \times 10^{-14}$	Hz s $^{-1}$
Spin frequency ν_{spin} [30]	$435.317993681(12)$	Hz
r -mode f_0 [9]	621.3034	Hz
$2\nu_{\text{spin}}$	870.63598	Hz

TABLE IV. Orbital and spin parameters of XTE J1751-305.

Frequency (Hz)	Strain (dimensionless)
435.3	3.2656×10^{-24}
621.3	4.7125×10^{-24}
870.6	7.7532×10^{-24}

TABLE V. Upper limits for 0.1 Hz frequency bands containing three possible putative signals from J1751-305. In increasing order of frequency, these are the ν_{spin} , r -mode, and $2\nu_{\text{spin}}$. The upper limits represent an average (random) polarization 95%-confidence limit, determined using 200 injections per observatory for each band.

B. XTE J1751-305 results

No evidence for GW emission from XTE J1751-305 is found in the frequency bands [434.5, 436.5] Hz, [620.5, 622.5] Hz, or [869.5, 871.5] Hz. No candidate templates passed both threshold and coincidence requirements between H1 and L1 observatories.

In the absence of any candidates, upper limits are set in Table V. We follow the same method as Section III B, with minor modifications: sky location, period, and projected semi-major axis are adjusted to fit J1751, and the frequency span is limited to the 0.1 Hz bands containing each of three possible emission frequencies: ν_{spin} , r -mode, and $2\nu_{\text{spin}}$. To our knowledge, these are the first limits set on J1751 using gravitational-wave data.

Debate [41, 42] over the existence of r -modes in J1751 motivates future searches. S6 amplitude spectral densities ranged around $[3 - 6] \times 10^{-23}$ Hz $^{-1/2}$ over [435, 870] Hz. In the same range, Advanced LIGO in O1 has achieved strain sensitivities of $[1 - 2] \times 10^{-23}$ Hz $^{-1/2}$ [43]; design sensitivity may achieve $[4 - 5] \times 10^{-24}$ Hz $^{-1/2}$ [44]. Extrapolating to equivalent duration design sensitivity data, we might anticipate approximately order-of-magnitude improvements in upper limits. Andersson *et al* [41] discuss how, with a nominal internal mode amplitude $\alpha = 10^{-3}$, the expected strain of an r -mode in LIGO might be approximately 1×10^{-24} . While internal

mode amplitude is also highly-uncertain, future upper limits could indeed be illuminating.

V. CONCLUSIONS

LIGO S6 data is analyzed for continuous gravitational wave emission from Sco X-1 using the TwoSpect method. While no credible detections are made, upper limits are set for randomly polarized gravitational waves from Sco X-1 from 40 to 2040 Hz. This analysis covers the uncertainty in projected semi-major axis, σ_{a_p} , over $\pm 3\sigma_{a_p}$ as was known in S6 [28], though σ_{a_p} ephemerides are evolving [29]. Upper limits for randomly polarized GWs are set for this 2-kHz frequency band, except for five 1-Hz disturbed bands. The best upper limit is $h_0 = 1.8 \times 10^{-24}$ at 165 Hz, 27 times the torque-balance limit there. XTE J1751-305 is also targeted and shows no sign of GW emission, although transients cannot be ruled out; we set the first upper limits on J1751 using GW data.

These results using TwoSpect [16, 18] are the best that span a 2 kHz frequency range and use initial LIGO data [17, 20–23]. In this paper, the frequency range surveyed is considerably larger than the [20, 57.25] Hz previously-analyzed by TwoSpect for S6 and Virgo VSR2/3 [17] or [50, 550] Hz analyzed by Sideband for S5 [23]. Moreover, in an advance over Radiometer S5 limits [21], the limits presented here are in physical units of strain h_0 (instead of h_{RMS}), for simulated random polarizations, at the 95%-confidence level. The relative performance of the pipelines is fairly consistent with that observed in the Sco X-1 Mock Data Challenge [19], allowing for differences in bin size and observation time for Radiometer and the Bayesian upper limit technique used for Sideband in S5. Already, as this paper shows, TwoSpect achieves a sensitivity depth of approximately $10 \text{ Hz}^{-1/2}$ (as previously estimated [18]; see Equation 9) with respect to the S6 amplitude spectral density. Extrapolated to an equivalent duration of Advanced LIGO design sensitivity data at an amplitude spectral density of $4 \times 10^{-24} \text{ Hz}^{-1/2}$, this method might set an upper limit of 4×10^{-25} on Sco X-1, well within an order of magnitude of the predicted torque-balance limit [5]. Promising pipelines are in development [45, 46], though further enhancement to the TwoSpect algorithm is also expected [38]. This method sets new upper limits on Sco X-1 GW emission using S6 data, and it is ready to be applied to data from Advanced LIGO, Advanced Virgo, and KAGRA.

ACKNOWLEDGMENTS

This work was partly funded by National Science Foundation grants NSF PHY-1505932 and NSF HRD-1242090 as well as by the Max-Planck-Institut. These investigations use data and computing resources from the LIGO Scientific Collaboration. Further thanks to the Albert-Einstein-Institut Hannover and the Leibniz Universität

Hannover for support of the Atlas cluster on which most of the computing for this project was done. The data used in this analysis is available through the LIGO Open Science Center [47]. Thanks to Maria Alessandra Papa, Reinhard Prix, and Chris Messenger for proofreading and suggestions, as well as to our referees for thorough reading and comments. This document bears LIGO Document Number DCC-P1500039.

Appendix A: Eccentricity

Eccentricity effects have not been analytically considered for this algorithm before. Starting from the instantaneous relative GW frequency offset $(\delta f)/f$ [32], with eccentric anomaly E , eccentricity e and argument of periapse ω ,

$$\left| \frac{\delta f}{f} \right| = a_p \Omega \left| \frac{\sqrt{1-e^2} \cos E \cos \omega - \sin E \sin \omega}{1-e \cos E} \right|. \quad (\text{A1})$$

Instantaneous frequency offsets result in shifted estimates of the apparent intrinsic frequency and modulation depth: labeling these offsets δf_a and $\delta \Delta f_a$,

$$\delta f_a = \frac{1}{2} |\max(\delta f) + \min(\delta f)|, \quad (\text{A2})$$

$$\delta \Delta f_a = \frac{1}{2} |\max(\delta f) - \min(\delta f)| - \Delta f_{\text{obs}}. \quad (\text{A3})$$

Extremizing over E to solve where $e \geq 0$, $e \ll 1$,

$$\frac{\delta f_a}{\Delta f_{\text{obs}}} = \left(\frac{\sqrt{1-e^2} \cos^2 \omega + \sin^2 \omega}{1-e^2 \cos^2 \omega} e \cos \omega \right), \quad (\text{A4})$$

$$\frac{\delta \Delta f_a}{\Delta f_{\text{obs}}} = \left(\frac{\sqrt{1-e^2} \cos^2 \omega + \sin^2 \omega}{1-e^2 \cos^2 \omega} \right) - 1. \quad (\text{A5})$$

The offsets are related by $\delta f_a = (\delta \Delta f_a + \Delta f_{\text{obs}}) e \cos \omega$. Equations A4 and A5 predict the $(f, \Delta f_{\text{obs}})$ position of $\max(R)$. A case is simulated at the edge of the Sco X-1 search parameter space, with $a_p = 1.95$ light-s, $f = 2039.95$ Hz; compared to when $e = 0$, the $e = 0.07$ simulation shows maximum shifts of $\delta f_a = -25.7$ mHz, $\delta \Delta f_a = +0.9$ mHz for $\omega = 0$ and $\delta f_a = +25.7$ mHz, $\delta \Delta f_a = +0.9$ mHz for $\omega = \pi$. This is consistent with predictions up to a sign, which depends on the convention for ω .

The R value computed for an injected signal with a simulated eccentricity σ_e is comparable to that when $e = 0$, so given the physical probability of orbital circularization, eccentricity will be treated as a problem in parameter estimation but not while setting upper limits.

Appendix B: Spin-wandering across frequency bins

Consider a gravitational-wave signal that changes in frequency f_0 by one frequency bin, width $1/T_{\text{coh}}$, during the observing time, T_{obs} . Model this change as linear in time; for example, consider an LMXB where accretion suddenly stopped, and the neutron star kept radiating GW at its torque-balance frequency f_0 . This model should set an upper limit. The limit is found by comparing the frequency bin width allowance to the spindown rate. The frequency bin width allowance is,

$$\frac{df_0}{dt} T_{\text{obs}} = -\frac{1}{T_{\text{coh}}}. \quad (\text{B1})$$

Comparing to the spindown rate of an isolated star [48],

$$\frac{dE}{dt} = -\frac{32}{5} \frac{G}{c^5} I_{zz}^2 \epsilon^2 (\pi f_0)^6, \quad (\text{B2})$$

$$h_0 = 4\pi^2 \frac{G I_{zz} f_0^2 \epsilon}{c^4 r}. \quad (\text{B3})$$

The first equation can be transformed by noting that $E = I_{zz}(\pi f_0)^2/2$, so

$$\frac{df_0}{dt} = \frac{1}{\pi^2 I_{zz} f_0}, \quad (\text{B4})$$

and we can readily solve for ϵ in terms of h_0 . Combining these solutions,

$$\frac{df_0}{dt} = -\frac{2c^3}{5GI_{zz}} r^2 h_0^2 f_0. \quad (\text{B5})$$

Using values of $I_{zz} = 10^{38}$ kg m² and $r = 2.7$ kpc,

$$\frac{df_0}{dt} = [-1.1 \times 10^{-9} \text{ Hz s}^{-1}] \left(\frac{h_0}{10^{-24}} \right)^2 \left(\frac{f_0}{100 \text{ Hz}} \right). \quad (\text{B6})$$

For a loud candidate, for example $h_0 = 4 \times 10^{-24}$ at 1312.45 Hz, this spindown rate is 2.4×10^{-7} Hz s⁻¹, equal to 95 Hz spindown over the 40.5 million second T_{obs} of S6. This is, respectively, 80 thousand or 34 thousand times larger than the width of, respectively, 840-s or 360-s SFTs. Moreover, for a signal well above the torque-balance limit, the linear spindown approximation might be valid.

Applying the same logic to a signal at the torque-balance limit,

$$\frac{df_0}{dt} = -1.1 \times 10^{-9} \text{ Hz s}^{-1} \left[\frac{3.5 \times 10^{-26}}{10^{-24}} \right]^2 \frac{600}{100}, \quad (\text{B7})$$

$$= -8.2 \times 10^{-12} \text{ Hz s}^{-1}, \quad (\text{B8})$$

or approximately 0.033 Hz spindown over S6. This is also wider than the width of either frequency bin, by a factor of approximately 28 for 840-s SFTs and 12 for 360-s SFTs. However, this is a worst-case scenario, and torque-balance is thought to be an equilibrium condition. The sudden spindown of a neutron star from torque-balance is not expected. Because the potential for spin-wandering effects is not completely negligible, however, this subject remains a topic of active investigation [49].

Appendix C: Full list of outliers

Please see Table VI for a full list of outlier clusters.

#	H1 f (Hz)	Δf_{obs} (Hz)	R	h_{rec}	$-\log_{10} p$	L1 f (Hz)	Δf_{obs} (Hz)	R	h_{rec}	$-\log_{10} p$	Follow-up
1	42.0125	0.0077	8.42e+02	6.60e-23	-5.98e+01	42.0113	0.0077	1.82e+02	1.52e-23	-1.59e+01	a
2	63.9946	0.0114	2.35e+03	6.49e-24	-1.94e+02	63.9946	0.0114	2.95e+02	3.66e-24	-2.18e+01	b
3	108.1006	0.0195	2.01e+03	2.46e-24	-6.84e+01	108.1012	0.0189	2.15e+02	9.08e-25	-9.81e+00	a
4	108.8673	0.0184	1.26e+03	1.55e-24	-7.42e+01	108.8685	0.0196	1.89e+03	1.55e-24	-1.07e+02	c
5	109.4732	0.0183	4.26e+02	1.05e-24	-1.97e+01	109.4726	0.0174	2.43e+02	9.29e-25	-1.07e+01	a
6	111.0202	0.0128	4.97e+03	2.07e-24	-3.63e+02	111.0214	0.0116	1.42e+02	8.09e-25	-7.75e+00	b
7	128.0149	0.0234	2.96e+05	4.31e-24	-1.55e+04	128.0149	0.0231	2.97e+02	1.12e-24	-1.41e+01	b
8	139.5190	0.0166	2.52e+02	6.93e-25	-1.34e+01	139.5179	0.0178	8.75e+03	1.72e-24	-5.14e+02	b
9	154.0411	0.0267	1.70e+03	9.73e-25	-8.01e+01	154.0423	0.0255	2.37e+02	6.64e-25	-9.09e+00	b
10	154.5571	0.0256	2.30e+02	5.89e-25	-7.96e+00	154.5560	0.0268	2.30e+02	6.61e-25	-7.82e+00	a
11	156.8167	0.0237	3.67e+02	6.71e-25	-1.51e+01	156.8179	0.0225	3.35e+03	1.27e-24	-1.70e+02	a
12	157.9946	0.0268	8.22e+02	8.10e-25	-3.71e+01	157.9935	0.0256	4.89e+02	7.79e-25	-2.13e+01	b
13	158.3673	0.0269	4.56e+02	6.98e-25	-1.98e+01	158.3685	0.0278	3.02e+02	6.91e-25	-1.09e+01	b
14	158.8619	0.0276	1.27e+03	8.93e-25	-5.72e+01	158.8619	0.0285	6.50e+02	8.37e-25	-2.71e+01	b
15	190.8000	0.0322	7.45e+02	9.48e-25	-2.39e+01	190.8012	0.0334	4.22e+02	8.97e-25	-1.34e+01	a
16	192.5482	0.0184	2.11e+03	1.12e-24	-1.28e+02	192.5470	0.0172	4.91e+02	8.13e-25	-2.79e+01	c
17	200.5298	0.0331	1.41e+03	1.42e-24	-4.21e+01	200.5310	0.0343	4.77e+02	1.01e-24	-1.35e+01	a
18	209.2839	0.0326	3.73e+02	8.42e-25	-1.30e+01	209.2827	0.0338	3.92e+03	1.33e-24	-1.54e+02	a
19	223.6625	0.0373	1.63e+03	9.31e-25	-6.02e+01	223.6637	0.0385	6.58e+02	1.28e-24	-1.77e+01	b
20	256.0327	0.0448	8.55e+02	8.63e-25	-2.82e+01	256.0327	0.0448	5.04e+02	8.48e-25	-1.44e+01	b
21	268.1399	0.0383	2.93e+02	6.57e-25	-7.99e+00	268.1405	0.0392	4.87e+02	1.03e-24	-1.34e+01	a
22	360.0028	0.0638	9.95e+03	3.94e-24	-4.00e+02	360.0014	0.0652	1.34e+04	8.41e-24	-4.58e+02	b
23	361.4792	0.0536	6.14e+02	1.58e-24	-2.60e+01	361.4792	0.0536	2.45e+02	1.29e-24	-1.01e+01	a
24	375.3653	0.0624	2.48e+02	1.17e-24	-9.33e+00	375.3653	0.0596	2.30e+02	1.33e-24	-8.03e+00	a
25	383.1903	0.0701	5.58e+02	1.28e-24	-2.10e+01	383.1917	0.0694	5.05e+02	2.27e-24	-1.82e+01	b
26	400.1000	0.0641	2.96e+11	1.88e-22	-1.42e+10	400.1000	0.0641	3.25e+02	1.71e-24	-1.14e+01	b
27	403.7778	0.0426	6.43e+04	4.05e-24	-3.73e+03	403.7792	0.0405	6.99e+12	5.20e-22	-4.12e+11	b
28	404.8000	0.0720	3.50e+04	3.46e-24	-1.55e+03	404.8000	0.0740	2.51e+09	7.33e-23	-9.36e+07	b
29	420.0111	0.0691	7.62e+03	3.74e-24	-2.76e+02	420.0097	0.0705	2.54e+03	2.60e-24	-9.06e+01	b
30	435.2556	0.0465	2.09e+02	1.06e-24	-9.24e+00	435.2569	0.0486	1.97e+02	1.23e-24	-8.26e+00	a
31	440.1000	0.0805	9.89e+02	1.55e-24	-3.83e+01	440.1014	0.0791	8.92e+02	1.85e-24	-3.45e+01	b
32	448.0861	0.0771	2.94e+02	1.14e-24	-9.14e+00	448.0875	0.0792	3.02e+02	1.56e-24	-9.45e+00	b
33	450.9569	0.0735	2.60e+02	1.18e-24	-8.39e+00	450.9542	0.0762	2.74e+02	1.48e-24	-8.16e+00	a
34	468.1000	0.0745	2.99e+02	1.40e-24	-9.77e+00	468.1000	0.0745	5.20e+02	1.60e-24	-1.82e+01	b
35	480.0167	0.0829	1.11e+03	1.98e-24	-3.68e+01	480.0194	0.0802	2.59e+03	3.26e-24	-8.27e+01	b
36	482.2069	0.0673	2.65e+02	1.23e-24	-8.90e+00	482.2042	0.0680	5.04e+02	1.83e-24	-1.91e+01	a
37	500.0722	0.0915	3.82e+02	1.41e-24	-1.09e+01	500.0722	0.0915	3.82e+02	1.69e-24	-1.12e+01	a
38	539.9583	0.0856	1.56e+03	2.35e-24	-5.01e+01	539.9556	0.0884	3.47e+02	1.71e-24	-9.64e+00	b
39	552.0417	0.1003	3.20e+02	1.45e-24	-8.37e+00	552.0417	0.0982	5.37e+04	5.97e-24	-1.77e+03	b
40	568.1000	0.0935	3.05e+04	4.44e-24	-9.99e+02	568.1000	0.0915	3.42e+02	1.81e-24	-9.86e+00	b
41	570.3514	0.0759	3.36e+02	1.47e-24	-1.07e+01	570.3528	0.0779	2.51e+02	1.62e-24	-7.99e+00	a
42	600.0042	0.0840	3.61e+02	1.67e-24	-1.03e+01	600.0042	0.0819	9.09e+02	2.95e-24	-2.93e+01	b
43	646.5264	0.0822	2.71e+02	1.57e-24	-8.02e+00	646.5264	0.0850	3.68e+02	2.02e-24	-1.14e+01	a
44	656.6431	0.0650	2.20e+02	1.48e-24	-7.85e+00	656.6458	0.0630	2.67e+02	1.86e-24	-1.01e+01	d
45	691.1500	0.0777	4.25e+02	2.87e-24	-1.47e+01	691.1514	0.0763	6.12e+02	3.21e-24	-1.99e+01	b
46	692.1653	0.1133	4.62e+02	2.50e-24	-1.19e+01	692.1653	0.1154	7.05e+02	3.13e-24	-2.06e+01	b
47	719.9819	0.0815	4.39e+02	2.19e-24	-1.33e+01	719.9806	0.0836	8.26e+02	4.59e-24	-2.65e+01	b
48	729.6000	0.0918	2.74e+03	3.11e-24	-1.02e+02	729.5986	0.0912	4.97e+02	2.55e-24	-1.54e+01	b
49	770.2250	0.1229	4.18e+02	2.04e-24	-1.02e+01	770.2264	0.1256	3.98e+02	2.46e-24	-8.51e+00	d
50	839.9417	0.1515	4.52e+02	2.46e-24	-8.13e+00	839.9403	0.1488	7.14e+02	3.36e-24	-1.57e+01	b
51	870.0042	0.0925	4.66e+02	2.46e-24	-1.41e+01	870.0069	0.0938	1.22e+06	2.15e-23	-4.20e+04	b
52	908.9139	0.1330	4.54e+02	2.52e-24	-9.78e+00	908.9125	0.1358	6.19e+03	6.16e-24	-1.62e+02	a
53	942.7431	0.0812	2.69e+02	2.87e-24	-7.77e+00	942.7458	0.0791	2.54e+02	2.75e-24	-7.80e+00	a
54	957.6972	0.0803	2.61e+02	2.24e-24	-8.04e+00	957.6958	0.0817	2.79e+02	2.88e-24	-8.47e+00	d
55	963.2042	0.1615	4.52e+02	2.58e-24	-8.11e+00	963.2069	0.1595	1.27e+05	1.36e-23	-3.17e+03	b
56	1022.9708	0.1232	5.92e+02	4.25e-24	-1.44e+01	1022.9681	0.1260	4.13e+02	3.31e-24	-9.01e+00	a
57	1033.9875	0.1870	4.40e+05	3.06e-23	-1.04e+04	1033.9861	0.1891	1.46e+03	4.77e-24	-3.02e+01	b
58	1091.4764	0.0928	3.03e+02	2.69e-24	-8.58e+00	1091.4750	0.0942	3.10e+02	3.40e-24	-8.48e+00	a
59	1098.2125	0.1343	4.30e+02	3.20e-24	-9.39e+00	1098.2139	0.1357	3.88e+02	3.72e-24	-7.82e+00	b
60	1147.6944	0.2051	1.51e+03	4.66e-24	-2.80e+01	1147.6944	0.2023	1.98e+03	5.76e-24	-3.76e+01	b
61	1166.1347	0.2098	4.29e+03	6.30e-24	-9.00e+01	1166.1347	0.2119	1.29e+04	9.09e-24	-2.51e+02	b
62	1171.0847	0.1996	4.91e+02	3.36e-24	-7.76e+00	1171.0833	0.1975	1.72e+03	5.38e-24	-3.46e+01	a
63	1190.6125	0.1740	4.59e+02	3.16e-24	-8.20e+00	1190.6111	0.1719	1.10e+03	4.88e-24	-2.33e+01	b
64	1216.0986	0.2176	5.74e+02	3.57e-24	-8.42e+00	1216.0972	0.2196	3.18e+03	6.72e-24	-6.27e+01	b
65	1306.6861	0.1454	4.95e+02	3.76e-24	-1.05e+01	1306.6847	0.1426	1.51e+08	1.02e-22	-3.90e+06	b
66	1312.4542	0.2373	5.86e+02	3.77e-24	-8.17e+00	1312.4528	0.2380	6.07e+02	4.53e-24	-8.08e+00	d
67	1318.7181	0.1625	4.24e+02	3.72e-24	-7.78e+00	1318.7194	0.1611	6.24e+02	4.67e-24	-1.31e+01	b

TABLE VI – *continued on next page*

TABLE VI – *continued from previous page*

#	H1 f (Hz)	Δf_{obs} (Hz)	R	h_{rec}	$-\log_{10} p$	L1 f (Hz)	Δf_{obs} (Hz)	R	h_{rec}	$-\log_{10} p$	Follow-up
68	1374.1000	0.1351	6.67e+02	4.17e-24	-1.55e+01	1374.1000	0.1330	1.54e+06	6.03e-23	-3.28e+04	b
69	1375.8167	0.2496	8.66e+06	7.85e-23	-1.60e+05	1375.8153	0.2509	9.71e+02	6.76e-24	-1.40e+01	b
70	1397.9347	0.1343	1.61e+03	5.09e-24	-4.25e+01	1397.9333	0.1356	6.32e+02	4.83e-24	-1.43e+01	b
71	1489.2181	0.2425	1.13e+03	4.95e-24	-1.80e+01	1489.2194	0.2418	5.96e+02	4.96e-24	-8.41e+00	b
72	1495.2931	0.2541	1.63e+04	9.75e-24	-3.03e+02	1495.2931	0.2568	9.95e+03	1.02e-23	-1.79e+02	b
73	1506.0250	0.1746	7.25e+02	4.44e-24	-1.41e+01	1506.0264	0.1767	5.38e+04	1.56e-23	-1.27e+03	b
74	1514.1667	0.2749	2.56e+04	1.09e-23	-4.50e+02	1514.1694	0.2756	7.15e+02	5.28e-24	-9.45e+00	b
75	1563.0278	0.2769	9.49e+02	5.04e-24	-1.26e+01	1563.0278	0.2796	6.74e+02	5.86e-24	-7.98e+00	b
76	1574.2778	0.2212	5.89e+02	4.50e-24	-8.53e+00	1574.2778	0.2226	1.31e+03	7.40e-24	-2.36e+01	b
77	1578.4389	0.2533	5.78e+02	4.50e-24	-7.81e+00	1578.4375	0.2561	4.26e+03	9.95e-24	-6.90e+01	b
78	1600.3236	0.1400	1.84e+03	6.02e-24	-4.90e+01	1600.3236	0.1428	4.13e+02	5.26e-24	-8.25e+00	b
79	1607.9000	0.1503	1.08e+04	9.48e-24	-2.90e+02	1607.9000	0.1476	4.63e+02	5.38e-24	-9.56e+00	b
80	1611.5097	0.1596	4.55e+02	4.27e-24	-8.86e+00	1611.5111	0.1582	5.75e+02	5.59e-24	-1.17e+01	b
81	1627.7389	0.2915	6.69e+02	4.75e-24	-7.99e+00	1627.7389	0.2887	8.37e+02	6.36e-24	-1.08e+01	a
82	1719.2667	0.2443	1.32e+06	4.43e-23	-2.68e+04	1719.2653	0.2429	5.50e+05	3.61e-23	-1.04e+04	b
83	1738.7639	0.1501	2.27e+06	4.87e-23	-5.90e+04	1738.7653	0.1473	4.15e+02	5.47e-24	-7.79e+00	b
84	1824.0167	0.1996	8.76e+08	1.88e-22	-1.89e+07	1824.0194	0.2016	5.26e+02	6.27e-24	-7.91e+00	b
85	1842.9083	0.1588	3.66e+03	8.23e-24	-9.06e+01	1842.9097	0.1615	4.50e+02	6.17e-24	-8.02e+00	b
86	1920.0792	0.1825	4.63e+02	5.14e-24	-7.97e+00	1920.0806	0.1853	4.92e+02	6.58e-24	-7.76e+00	b
87	1940.8569	0.1655	5.97e+02	5.51e-24	-1.22e+01	1940.8583	0.1683	4.59e+02	6.19e-24	-7.85e+00	b
88	1976.2778	0.2913	2.81e+04	1.47e-23	-4.64e+02	1976.2792	0.2886	6.62e+02	7.06e-24	-8.03e+00	a
89	2005.5792	0.2230	6.26e+02	5.88e-24	-9.18e+00	2005.5778	0.2216	1.46e+04	1.54e-23	-2.75e+02	b
90	2007.7694	0.3526	2.77e+03	8.57e-24	-3.74e+01	2007.7694	0.3526	8.51e+02	7.55e-24	-9.18e+00	b

TABLE VI: All clustered outliers from the Sco X-1 search. Follow-up codes: (a), broad disturbance found in amplitude spectral density (ASD) (b), sharp lines found in ASD; (c), corresponds to known injected signal; (d), followed-up with coherent-summing in Table III.

- [1] P.R. Brady, T. Creighton, C. Cutler, and B.F. Schutz, “Searching for periodic sources with LIGO,” *Phys. Rev. D* **57**, 2101 (1998).
- [2] J. Papaloizou and J.E. Pringle, “Gravitational radiation and the stability of rotating stars,” *MNRAS* **184**, 501 (1978).
- [3] R.V. Wagoner, “Gravitational radiation from accreting neutron stars,” *Ap. J.* **278**, 345 (1984).
- [4] R. Giacconi, H. Gursky, F.R. Paolini, and B.B. Rossi, “Evidence for X rays from sources outside the solar system,” *Phys. Rev. Lett.* **9** (1962).
- [5] L. Bildsten, “Gravitational radiation and rotation of accreting neutron stars,” *Astrophys. J. Lett.* **501**, L89 (1998).
- [6] N. Andersson, “A new class of unstable modes of rotating relativistic stars,” *APJ* **502**, 708 (1998).
- [7] J.L. Friedman and S.M. Morsink, “Axial instability of rotating relativistic stars,” *APJ* **502** (1998).
- [8] B.J. Owen *et al.*, “Gravitational waves from hot young rapidly rotating neutron stars,” *Phys. Rev. D* **58**, 084020 (1998).
- [9] T. Strohmayer and S. Mahmoodifar, “A non-radial oscillation mode in an accreting millisecond pulsar?” *Astrophys. J* **784** (2014), 10.1088/0004-637X/784/1/72.
- [10] P. Jaranowski, A. Królak, and B. Schutz, “Data analysis of gravitational-wave signals from spinning neutron stars: the signal and its detection,” *Phys. Rev. D* **58**, 063001 (1998).
- [11] Badri Krishnan, Alicia M. Sintes, Maria Alessandra Papa, Bernard F. Schutz, Sergio Frasca, and Cristiano Palomba, “Hough transform search for continuous gravitational waves,” *Phys. Rev. D* **70**, 082001 (2004).
- [12] B. Abbott, *Phys. Rev. D* **77**, 022001 (2008).
- [13] B. Abbott *et al.*, “All-sky LIGO search for periodic gravitational waves in the early fifth-science-run data,” *Phys. Rev. Lett* **102**, 111102 (2009).
- [14] V. Dergachev, “On blind searches for noise dominated signals: a loosely coherent approach,” *Class. Quant. Grav.* **27**, 205017 (2010).
- [15] J. Abadie *et al.*, “All-sky search for periodic gravitational waves in the full S5 LIGO data,” *Phys. Rev. D* **85**, 022001 (2012).
- [16] E. Goetz and K. Riles, “An all-sky search algorithm for continuous gravitational waves from spinning neutron stars in binary systems,” *Class. Quant. Grav.* **28**, 215006 (2011).
- [17] J. Aasi *et al.*, “First all-sky search for continuous gravitational waves from unknown sources in binary systems,” *Phys. Rev. D* **90**, 062010 (2014).
- [18] G.D. Meadors, E. Goetz, and K. Riles, “Tuning into scorpius x-1: adapting a continuous gravitational-wave search for a known binary system,” *Class. Quant. Grav.* **33**, 105017 (2016).
- [19] C. Messenger, H. J. Bulten, S. G. Crowder, V. Dergachev, D. K. Galloway, E. Goetz, R. J. G. Jonker, P. D. Lasky, G. D. Meadors, A. Melatos, S. Premachandra, K. Riles, L. Sammut, E. H. Thrane, J. T. Whelan, and Y. Zhang, “Gravitational waves from scorpius x-1: A comparison of search methods and prospects for detection with advanced detectors,” *Phys. Rev. D* **92**, 023006 (2015).

- [20] B. Abbott *et al.*, “Searches for periodic gravitational waves from unknown isolated sources and Scorpius X-1: results from the second ligo science run,” *Phys. Rev. D* **76**, 082001 (2007).
- [21] J. Abadie *et al.*, “Directional limits on persistent gravitational waves using LIGO S5 science data,” *Phys. Rev. Lett.* **107**, 271102 (2011).
- [22] L. Sammut, C. Messenger, A. Melatos, and B.J. Owen, “Implementation of the frequency-modulated sideband search method for gravitational waves from low mass x-ray binaries,” *Phys. Rev. D* **89**, 043001 (2014).
- [23] J. Aasi *et al.*, “Directed search for gravitational waves from Scorpius X-1 with initial LIGO data,” *Phys. Rev. D* **91**, 062008 (2015).
- [24] C.F. Bradshaw, E.B. Fomalont, and B.J. Geldzahler, “High-resolution parallax measurements of Scorpius X-1,” *ApJ* **512**, L121 (1999).
- [25] M. F. Skrutskie *et al.*, “The Two Micron All Sky Survey (2MASS),” *The Astronomical Journal* **131**, 1163–1183 (2006).
- [26] A.L. Watts, B. Krishnan, L. Bildsten, and B.F. Schutz, “Detecting gravitational wave emission from the known accreting neutron stars,” *MNRAS* **389**, 839 (2008).
- [27] D. K. Galloway, S. Premachandra, D. Steeghs, T. Marsh, J. Casares, and R. Cornelisse, “Precision Ephemerides for Gravitational-wave Searches. I. Sco X-1,” *Ap J* **781**, 14 (2014), arXiv:1311.6246 [astro-ph.HE].
- [28] D. Steeghs and J. Casares, “The Mass Donor of Scorpius X-1 Revealed,” *Astrophys. J.* **568**, 273–278 (2002), astro-ph/0107343.
- [29] L. Wang, D. Steeghs, and D. Galloway, “Sco X-1 parameters summary,” private communication (2016).
- [30] C.B. Markwardt *et al.*, “Discovery of a second millisecond accreting pulsar: XTE J1751-305,” *Astrophys. J.* **575**, L21–L24 (2002).
- [31] A. Riggio, L. Burderi, T. Di Salvo, A. Papitto, A. D’Ai, R. Iaria, and M.T. Menna, “Secular spin-down of the AMP XTE J1751-305,” *A&A* **531**, A140 (2011).
- [32] Paola Leaci and Reinhard Prix, “Directed searches for continuous gravitational waves from binary systems: Parameter-space metrics and optimal scorpius x-1 sensitivity,” *Phys. Rev. D* **91**, 102003 (2015).
- [33] B. Behnke, M.A. Papa, and R. Prix, “Postprocessing methods used in the search for continuous gravitational-wave signals from the Galactic Center,” *PRD* **91**, 064007 (2015).
- [34] C. Messenger, R. Prix, and M.A. Papa, “Random template banks and relaxed lattice coverings,” *Phys. Rev. D* **79**, 104017 (2009).
- [35] J. Abadie *et al.*, “Calibration of the LIGO gravitational wave detectors in the fifth science run,” *NIM-A* **623**, 223–240 (2010).
- [36] G.J. Feldman and R.D. Cousins, “Unified approach to the classical statistical analysis of small signals,” *Phys. Rev. D* **57**, 3873 (1998).
- [37] J. Aasi *et al.*, “Characterization of the LIGO detectors during their sixth science run,” *Class Quant Grav* **32**, 115012 (2015).
- [38] E. Goetz and K. Riles, “Coherently combining data between detectors for all-sky semi-coherent continuous gravitational wave searches,” *Class Quant Grav* **33**, 085007 (2016).
- [39] C. Cutler and B.F. Schutz, “Generalized F-statistic: Multiple detectors and multiple gravitational wave pulsars,” *Phys Rev D* **72**, 063006 (2005).
- [40] J. Aasi *et al.*, “Einstein@home all-sky search for periodic gravitational waves in LIGO S5 data,” *Phys Rev D* **87**, 042001 (2013).
- [41] N. Andersson, D.I. Jones, and W.C.G. Ho, “Implications of an r mode in XTE J1751-305: mass, radius and spin evolution,” *Mon. Not. R. Astr. Soc.* **442**, 1786–1793 (2014).
- [42] U. Lee, “Excitation of a non-radial mode in a millisecond X-ray pulsar XTE J1751-305,” *Mon. Not. R. Astr. Soc.* **442**, 3037–3043 (2014).
- [43] B.P. Abbott *et al.* (LIGO Scientific Collaboration and Virgo Collaboration), *Phys. Rev. Lett.* **116**, 061102 (2016).
- [44] G.M. Harry *et al.*, “Advanced LIGO: the next generation of gravitational wave detectors,” *Class. Quant. Grav.* **27**, 084006 (2010).
- [45] Sanjeev Dhurandhar, Badri Krishnan, Himan Mukhopadhyay, and John T. Whelan, “Cross-correlation search for periodic gravitational waves,” *Phys. Rev. D* **77**, 082001 (2008), arXiv:0712.1578.
- [46] John T. Whelan, Santosh Sundaresan, Yuanhao Zhang, and Prabath Peiris, “Model-based cross-correlation search for gravitational waves from scorpius x-1,” *Phys. Rev. D* **91**, 102005 (2015).
- [47] LIGO Scientific Collaboration, “LIGO Open Science Center release of S6,” (2015), [DOI: 10.7935/K5RN35SD].
- [48] K. Riles, “Gravitational waves: sources, detectors and searches,” *Prog. in Particle & Nucl. Phys.* **68**, 1 (2013).
- [49] A. Mukherjee, C. Messenger, and K. Riles, “in prep.” .